Invited Paper

Metamaterials: paving the way for terahertz technology

Jianqiang Gu [1*] , Jiaguang Han [1], Zhen Tian [1], Chunmei Ouyang [1], Mingxia He [1] and Weili Zhang [1, 2]
[1] Center for Terahertz waves and College of Precision Instrument and Optoelectronics Engineering, Tianjin University, and the Key Laboratory of Optoelectronics Information and Technology (Ministry of Education), Tianjin 300072, China
[2] School of Electrical and Computer Engineering, Oklahoma State University, Stillwater, Oklahoma 74078, USA
[*1] Email: gjq@tju.edu.cn

(Received January 2, 2013)

Abstract: As a new branch of artificial devices, metamaterials have attracted numerous interest in interdisciplinary research fields. The profound scientific significance and ingenious functionalities of metamaterials present state of the art of factitious components. Especially, in the terahertz regime, metamaterials are comprehensively exploited as various terahertz functional components, which pave a way to supporting the development of the rising terahertz technology. Here, a number of metamaterial based functioning terahertz devices are reviewed, including advanced passive components and active geometries. Their design, fabrication, verifications, functionalities, and physical interpretations are presented. The prospective applications of terahertz metamaterials and their challenges are also discussed.

Keywords: Terahertz, Metamaterials, Time-domain spectroscopy

doi: 10.11906/TST.066-094.2013.03.05

In the electro-magnetic spectrum, terahertz radiation fills the gap between the microwave and infrared regimes. It covers the frequency range from 100 *GHz* up to 10 *THz*, corresponding to the vacuum wavelength range of 3000-30 μm [1,2]. Beginning end of last Century, the generation and detection of terahertz radiation has extensively progressed adopting both optical and electronic methods. Much attention has been paid to numerous terahertz application potentials. Terahertz technology has shown uniqueness and importance in security check [3-5], medical imaging [6-10], quality control [11], environment investigations [11-14], material science research [15-18], and so on. However, comparing to the neighboring microwave and infrared regimes, terahertz technology is still far less developed, which is not only reflected in the lack of high power terahertz sources and highly sensitive terahertz detectors, but also in the short of various terahertz devices used to control and manipulate terahertz radiation. High quality terahertz devices would largely extend the functionality of typical terahertz systems, such as terahertz time-domain spectroscopy (THz-TDS), for example. Thus they are essential in developing wide spread applications of terahertz technology. The challenges ahead of terahertz researchers mainly come from two facts: firstly, the low power of existing terahertz sources proposes strict requirements on terahertz devices. For example, the reflection on the interface of a device is usually tolerable at microwave and optical frequencies. In the terahertz regime, however, this is quite a big deal because several reflections may lower the signal down to the detection limit. The second fact is that natural materials do not exhibit strong magnetic or electric responses at terahertz frequencies, for example, at 1-3 *THz* [19]. The resonant response of conventional magnetic materials occurs at microwave frequencies, while the plasma frequency in natural metals is observed beyond the mid-infrared range. So there is rare natural material exhibiting strong terahertz magnetic or electric responses. This means that it is impossible to satisfactorily meet the requirement of terahertz devices only using nature materials.

To overcome these problems, artificial structures such as photonic crystals [20-23], surface plasmon structures [23-32] and metamaterials [33-39] have been considering as competent candidates of terahertz devices. Among these artificial materials, metamaterial has stimulated much research enthusiasm. Different from other artificial structures, the unit cell dimension of metamaterials is much smaller than the working wavelength, endowing metamaterials meaningful effective permittivity and permeability [40-42]. On the other hand, characterized by split-ring resonators (SRRs) and fishnet structures, metamaterials deliver strong electrical and even magnetic responses in the terahertz domain, which facilities the novel control of electromagnetic radiation such as negative refraction [43], abnormal Doppler effect [44] and cloaking [45-53]. The fancy features of metamaterials are counted on to fill the terahertz device gap. In addition, the feature size of terahertz metamaterials is on the order of micrometers, thus the two-dimensional (2D) metamaterial fabrication is utilizing a typical traditional photolithography process.

Since the first demonstration of magnetic terahertz response of metamaterials by T. Yen in 2004 [33], the tempting features of terahertz metamaterials have been numerously investigated. Until now, metamaterial based terahertz devices have involved negative refraction components, spectral filters, slow light devices, invisibility cloaks and polarizer components. What is more, selected semiconductors, superconductors and phase-swift oxides such as GaAs, silicon on sapphire (SOS), InSb, YBCO, NbN and VO_2 have been exploited as control materials for active metamaterial tuning [19, 54-62]. The electrical and magnetic responses of these active metamaterials can be tuned by external stimulations in terms of electric voltage, magnetic field, temperature and optical pump, greatly extending the flexibility of metamaterial devices. In this article, we present a review of a number of recent terahertz matemετerial work characterized by THz-TDS. The presentation is organized as follows: in Section II, we describe experimental methods used in terahertz metamaterial investigation and the fabrication process of terahertz metamaterials. In Section III, we review several passive metamaterial based terahertz devices. The active terahertz metamaterials are presented in Section IV. Finally, a conclusion is drawn in Section V.

II. Experimental methods

A. Terahertz time domain spectroscopy

Broadband transmission THz-TDS and some of its varieties were employed to investigate the terahertz metamaterial structures [23, 62, 63]. A typical photoconductive switch-based THz-TDS system was comprised of a GaAs transmitter, a SOS dipole antenna receiver, parabolic mirrors, and/or flat reflecting mirrors. A self mode-locked Ti:sapphire laser capable of generating 88-*MHz*, 800-*nm*, and 26-*fs* ultrafast optical pulses was used to gate the photoconductive switches with 10-*mW* average power on both the transmitter and receiver. For most metamaterial structures, the transmission setup was aligned in an 8-F confocal geometry, thus delivering an ideal beam coupling between the transmitter and receiver and a compressed terahertz beam of a 3.5-*mm* frequency-independent diameter. Such system has a useful bandwidth of 0.1 to 4.5 *THz* (3 *mm*-67 *μm*) and a SNR > 15000:1. All the varieties of 8-F THz-TDS will be introduced when the related work is presented.

In the transmission measurements, the metamaterial sample was placed midway between the transmitter and receiver modules right at the waist of the terahertz beam. The terahertz radiation penetrated the metamaterial at normal incidence with P-polarized electric field. A blank slab identical to the metamaterial substrate was used as a reference. The transmitted terahertz electric field through the sample and reference was recorded in time domain and then Fourier transformed into frequency-dependent amplitude spectra as $\tilde{E}_t(\omega)$ and $\tilde{E}_r(\omega)$, respectively. The absolute amplitude transmission of the array was defined as $T(\omega)=\left|\tilde{t}(\omega)\right|=\left|\tilde{E}_t(\omega)/\tilde{E}_r(\omega)\right|$ and the corresponding phase change was obtained through the relation $\varphi(\omega)=\arg\left[\tilde{t}(\omega)\right]$.

B. Sample fabrication

The minimum feature size of terahertz metamaterial structures is at the micrometer order. Thus conventional photolithography and metallization processes are suitable for most terahertz metamaterials. According to different purposes and utilizations, the patterned materials and the substrates are also different, which will be explained in each single work in Sec. III and IV. The photolithographic processing included spin coating of positive photoresist, convection oven bakes, contact mode exposure, resist development, wet or dry etch, thermally metallization and wafer slicing processes and so on. Other special fabrication process will be introduced in detail when the related work is referred to.

Section III Passive metamaterial based terahertz devices

A. Negative refraction terahertz metamaterial

Realization of negative refraction which predicted by Veselago in 1960*s* is the first milestone in the metamaterial research [64]. Negative index metamaterial has become an excellent platform for demonstrating unusual electromagnetic properties, such as superlens, abnormal Doppler Effect, and abnormal Cherenkov radiation. Negative refractive index was firstly realized at microwave frequencies using an SRR and rod array combination. Its in-plane incidence requirement is not suitable when moving to the terahertz regime because of the difficulties in the sample fabrication and experimental verification. Generally, terahertz negative refraction metamaterial adopts a sandwich arrangement consists of two patterned metal layer squeezing a dielectric spacer [65-68]. A typical example is a close-ring pair (CRP) metamaterial as shown in Fig. 1(a) [68]. An h = 22 μm thick isotropic Mylar film is sandwiched between an aligned pair of square close rings of 200 *nm* thickness. This freestanding sample was fabricated by a self-alignment process which is explained as follows: a layer of Al close rings was first patterned on Mylar by conventional photolithography using positive photoresist followed by metallization and lift-off process. The resulting ring pattern was subsequently used as a photomask to create an identical structure on the other side of Mylar with a negative photoresist, and followed again by lift-off process, thus establishing the final CRP structure. With a 22 μm thick Mylar spacer, the samples are not only freestanding but also flexible, which is very useful for many applications.

Transmission response of the CRP metamaterials was characterized under normal incidence using a typical 8-F THz-TDS. The solid curve in Fig. 1(b) shows the frequency-dependent amplitude transmission of a CRP metamaterial. Compared to the ring array (dashed curve) patterned only on one side of Mylar, the CRP metamaterial reveals a new transmission peak at 0.69 *THz*. Figures 1(c) and (d) present the spectral behaviors of effective permittivity and permeability obtained through ε_{eff} and μ_{eff} of the CRP metamaterial through the S_{11} and S_{21} parameters, which were obtained by the simulation of a single layer of CRP sample with 25-μm air spacers both in front of and behind it. Both ε_{eff} and μ_{eff} change dramatically around the resonance 0.69 *THz* and exhibit a distinct double negative behavior. The refraction index was obtained by $n_{eff} = -\sqrt{\varepsilon_{eff}\mu_{eff}}$ in which we must choose the minus root when both ε_{eff} and μ_{eff} are in negative domain. At 0.69 and 0.76 *THz* the index of refraction approaches -2.8 and -1.0, respectively. Such resonant properties are well reproduced by numerical simulation (dotted curve). The negative refraction of the MDM structure lays in the electrical and magnetic resonance responses to the incidence wave, which is clearly illustrated in Fig. 1(a). The current in each horizontal arm of the ring provides the electrical resonance, giving a negative permittivity. Different from this, the anti-symmetric current in the ring pair, induced by the incident magnetic field in the dielectric spacer, together with the displacement current between them form a loop and result in negative permeability at the resonance frequency.

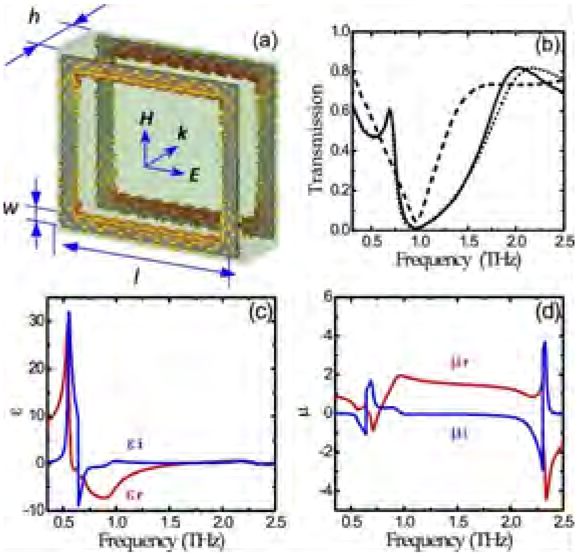

Fig. 1 (a) Schematic of a CRP unit cell with typical dimensions of $l = 60\ \mu m$, $w = 5\ \mu m$, and $h = 22\ \mu m$. The arrows in the rings represent surface current induced at the resonance frequency. (b) Measured (solid curve) and simulated (dotted curve) of a single-layer CRP metamaterial. The dashed curve illustrates the measured transmission of corresponding Al rings patterned only on one side of Mylar. (c) and (d) are the retrieved real part (red line) and image part (blue line) permittivity and permeability of the CRP metamaterials, respectively [68] .

The potential application of negative index material, such as superlens and abnormal Doppler devices can not be well investigated by single layer metamaterial. To form a bulk negative index metamaterial, we stacked the CRP layers with 50 μm thick Mylar spacer and investigated the resulted transmission of these multilayer CRP samples. As shown in Fig. 2, the negative refraction peak resonance exhibits an improved contrast though the absolute transmission amplitude decreases due to material loss. Importantly, we found that the misalignment between the different CRP layers does not significantly influence the resonance behavior. This robust feature will be very useful when building a bulk CRP metamaterial.

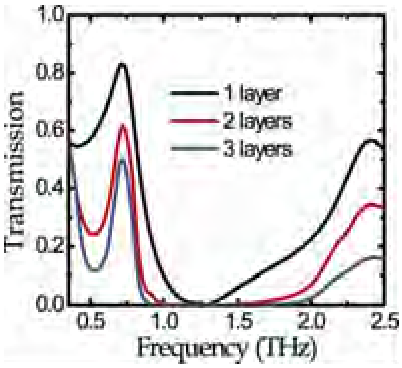

Fig. 2 Measured transmissions of multi-layer CRPs. A Mylar film of 50 μm is used as the spacer in the multilayer CRPs [68].

B. Metamaterial based terahertz filters

Besides negative refraction, metamaterials have also been exploited extensively as terahertz filters [69-74]. A typical example is a SRR array, which naturally serves as a transmission band stop filter with a higher Q factor compared to the bar array. Except band stop filters, more attentions have recently been paid to band pass filters using terahertz metamaterials, which has very high application values in terahertz signal modulation. Interestingly, we found the complementary of the CRP structure mentioned above is a promising candidate to realize broadband bandpass filter [74]. Figure 3(a) illustrates the schematic of the unit cell of the CRP complementary with normally incident electromagnetic field. A pair of 200-*nm* thick CRP complementary structure layers sandwiches a dielectric layer of thickness *d*.

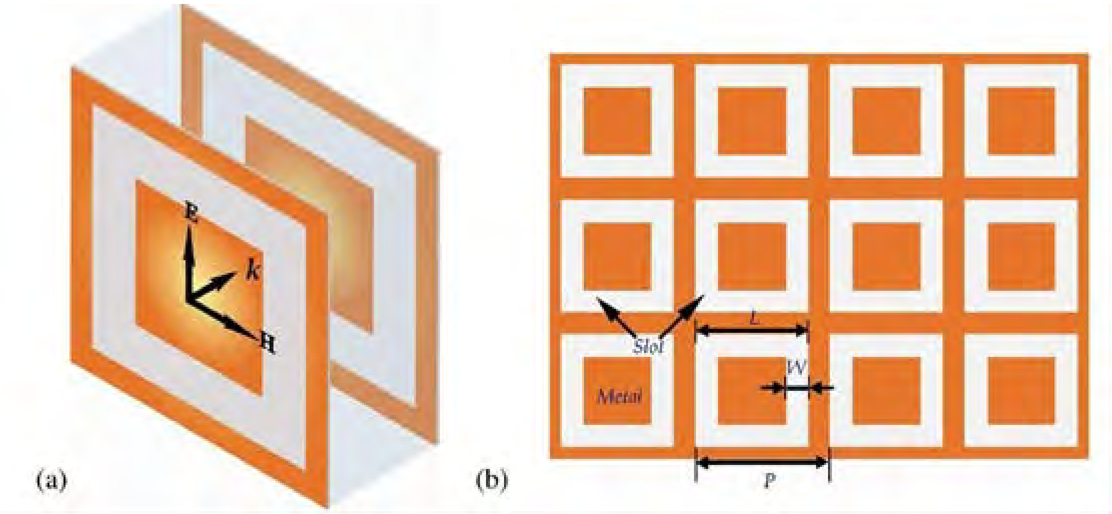

Fig. 3 (a) The unit cell of the sandwich metal-dielectric-metal structure with normal incident electromagnetic field. (b) Schematic of a square array of square-loop-shaped slots with a period of *P*, linewidth *W* and length *L*. The thickness of the middle dielectric substrate is d [74].

Figure 3(a) shows the simulated transmission of a typical metal-dielectric-metal (MDM) structure with dimensional parameters: $P = 120\ \mu m$, $L = 100\ \mu m$, $W = 20\ \mu m$ and $d = 21\ \mu m$, where the simulated model assumes that the metal is chosen as Aluminum and the middle dielectric is Mylar of relative permittivity $\varepsilon_{\rm d} = 2.89$. For comparison, a metal-dielectric (MD) structure with only one single metallic layer of the same square-loop hole array as that in MDM is also presented by the blue curve. Inspection of the transmission clearly shows that the MDM structure of double metallic layers has a much flatter transmission top as compared to that in MD. Clearly, the additional second array has the significant effect of flattering the transmission top and thus leads to an broad passband. The resonance top in the MDM structure is pulled broadly by the two resonance frequency $f_{\rm i} = 0.95\ THz$ and $f_{\rm a} = 1.28\ THz$ away from each other, and the simulated passband response centers at $f_0 = 1.12\ THz$.

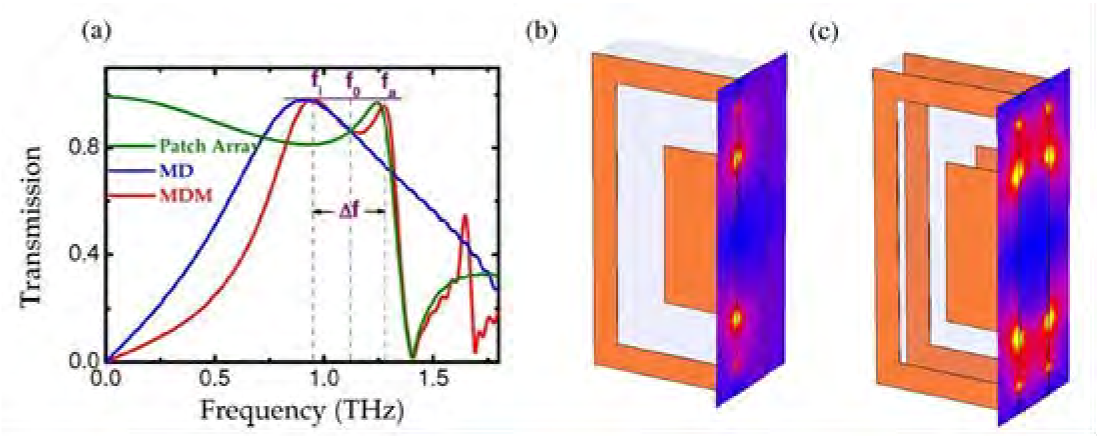

Fig. 4 (a) Comparison of the transmission spectra of the chosen MDM with the MD structure of only one single metallic layer, as well as the sandwich patch array. (b) and (c) are electric field distributions at lower resonance frequency for the MD and MDM structures, respectively [74] .

For our case, we noticed that lower resonance frequency f_i is located near the resonance frequency of the MD structure, as shown in Fig. 4(a). The excitation of the surface plasmons by the periodically arranged slot arrays in the MD structure is considered to be responsible for this resonance peak. The electric field distributions in Fig. 4(b) also represent this feature clearly. The resonance f_i occurs in the single-layer MD structure. On the other hand, however, f_a is located at a higher frequency. When we search the origin of the resonance f_a, it is interesting to notice that the resonance f_a is close to the resonance frequency excited in the patch array, as shown in Fig. 4(a). The localized electrical field is excited in the metallic patch in each plane, and when two-metallic-patch interfaces are brought together, the resonance modes around each interface start to interact and couple together and thus produces the resonance f_a. The coupling between the front and back patch can be seen obviously through the electric field distributions in Fig. 4(c).

The complementary CRP structure could realize a broad pass band. But this pass band shrinks when designed f_0 red shifts to low frequency. To realize a ultrawide band pass filter below 1 *THz*, a bilayer meander-line structure was adopted as shown in Fig. 5(a) and (b) [69]. Two layers of metallic meander-lines above and below an isolating dielectric film are identical in all respects except that the upper layer is rotated over the lower layer by 90° with respect to the normal axis (designated as the z axis). The lower-layer metallic meander-lines, made from 0.2 μm thick aluminum with dimensions w = 10 μm and l = 40 μm were first fabricated using conventional photolithography on a silicon substrate of thickness d = 640 μm. The isolating dielectric layer made from polyimide with a thickness h = 20 μm was spun coated on the meander-lines. Finally, the upper-layer meander-lines were fabricated on top of the polyimide film using aligned photolithography. Two other meander-line metamaterial were also fabricated, with all geometric parameters (except the substrate thickness d) multiplied by a factor r = 1.2 and 1.6 with respect to the first sample.

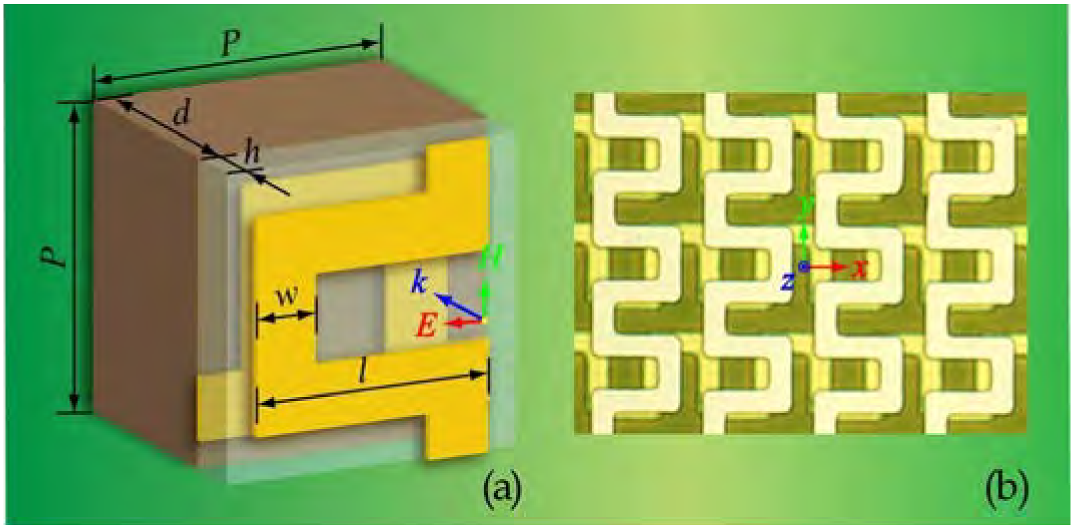

Fig. 5 (a) Three-dimensional schematic of the unit cell of the meander-line metamaterial. (b) View of the sample from the +*z* axis [69].

Figure 6(a) illustrates the transmission spectra $T(\omega)$ for all three meander-line samples (r = 1, 1.2, 1.6). The flat passbands $f \in [0.52, 1.65]\,THz$ for r=1, $f \in [0.42, 1.31]\,THz$ for r=1.2 and $f \in [0.34, 0.95]\,THz$ for r = 1.6 can be easily identified. The average insertion loss is as low as around 3 *dB*; it can be further enhanced by replacing aluminum with a noble metal and the polyimide with a dielectric medium of lower loss. The edges of each passband fall off at a rate greater than 50 *dB/THz* to the rejection bands, which are less than 15 *dB* throughout the spectral regime of interest. The passband ripples are within 1 *dB* across the 1 *dB* bandwidth, and the quality factors of all three filters are approximately the same. Though finally with increasing r factor, the central frequency of the meander-line structure is found to red shift with a narrower 3 *dB* bandwidth. But clearly, this bilayer metamaterial present a promising functionality as a terahertz bandpass filter, especially below 1 *THz*.

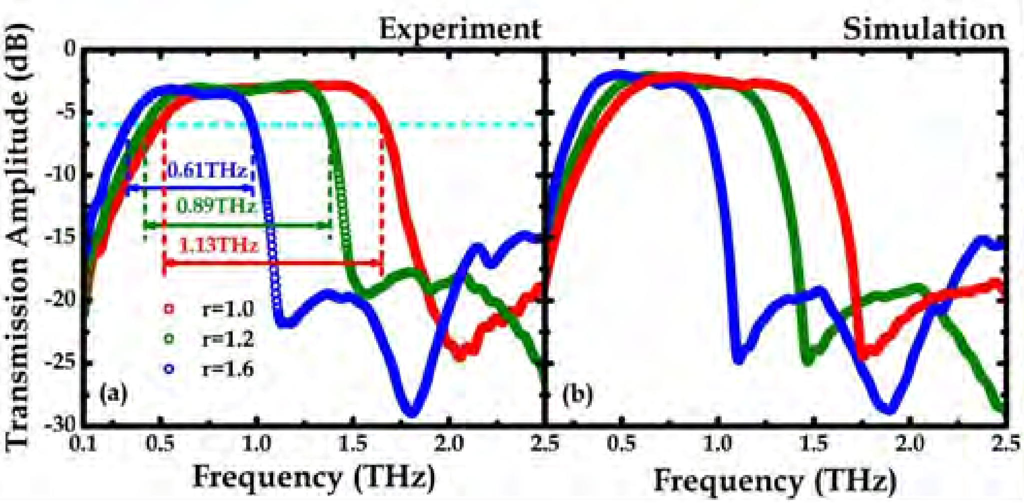

Fig. 6 (a) Measured (open circles) and (b) simulated spectra of $T(\omega)$ for all three metamaterial samples [69].

Incidence angle dependence is an important parameter for normally utilized terahertz filter, which directly decide its application promise. Transmission measurements were also carried out for oblique incidence characterized by an angle θ between the wave vector of the incident terahertz wave and z axis. The measured transmission coefficients $T(\omega)$ are shown in Fig. 7 for $\theta = 0°, 5°, 15°, 30°$, and 45°, respectively. The transmission remains virtually insensitive to the incidence angle, suggesting robustness against the misalignment problems.

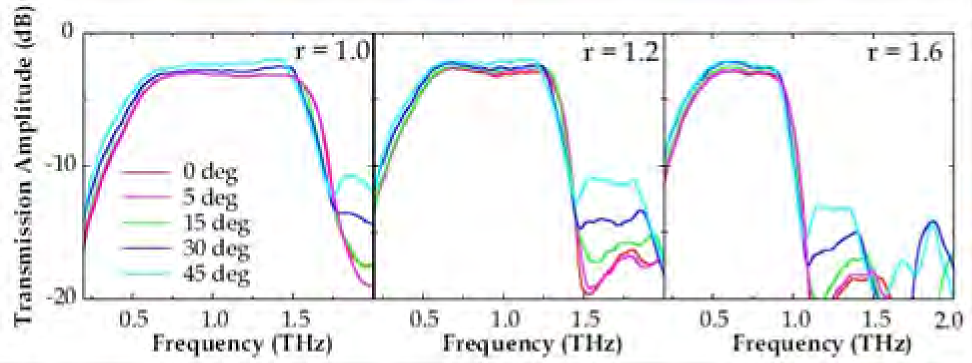

Fig. 7 Measured spectrums of $T(\omega)$ of all three meander-line structures for $\theta = 0°, 5°, 15°, 30°$, and 45°[69].

C. Metamaterial induced transparency structure as terahertz slow light devices

Slow light effect in high dispersive devices is an attractive phenomenon. In visible light regime, slow light devices have been extensively studied. On one hand, slow light phenomenon is used as optical fiber delay line and optical buffer, both of which are very important in all-optical communications. On the other hand, the high dispersion in slow light device has great potential in ultra-sensitive sensing. Back to the terahertz regime, slow light has been achieved in metamaterial structures and photonic crystals. Especially, metamaterial induced transparency, which is a metamaterial analogue of electromagnetically induced transparency (EIT) phenomenon in quantum optics, was predicted as a high quality slow light device with group refractive index [75-83]. Furthermore, the sharp EIT-like resonance in metamaterials can be exploited as promising sensing devices. Thus, there is enormous interest recently in the classical EIT phenomenon due to its multifunctional applications.

In general, the EIT-like spectral response in metamaterials is a result of destructive interference between the bright and dark mode resonances. The bright mode usually possesses a low quality factor (Q) due to its superradiant nature and the dark mode has a high Q since it is subradiant. A simple but typical metamateraial EIT analogue consists of a pair of SRRs symmetrically placed on the left and right side of a cut wire, as illustrated in Fig. 8(a) [75]. The incident electric field E is oriented along the y axis. Figure 8(b) shows a sole-wire array (left inset) that exhibits a typical localized surface plasmon (LSP) resonance at 0.67 *THz* (solid curve). However, in this case, the LC resonance in the sole-SRR pair (right inset) cannot be excited directly due to the structural symmetry with respect to the exciting field. With E along the x axis, on the other hand, a sharp

LC resonance is easily excited in the sole SRR pair (dotted curve) at exactly the same frequency as that of the LSP resonance in the wire array. As a result, when these two types of resonators are coupled together by arranging them in close proximity to each other within a unit cell, a typical EIT like spectral response is observed with the *y* polarized *E* field excitation, as shown in Fig. 8(c). In this design, the wire array can be excited directly by the incident electric field, acting as the bright resonator, while the fundamental LC resonance in the SRRs cannot be excited by the incident *E* field, thus acting as the dark mode. It is the destructive interference between the bright and dark resonators that gives rise to a strong EIT effect, leading to a sharp transparency window at 0.67 *THz*.

To verify the slow light ability, we retrieved the frequency dependent group refractive indices (n_g) for different SRR positions. The group index for δy = -28 *μm* has the value of 24 at the peak of the EIT transparency window.

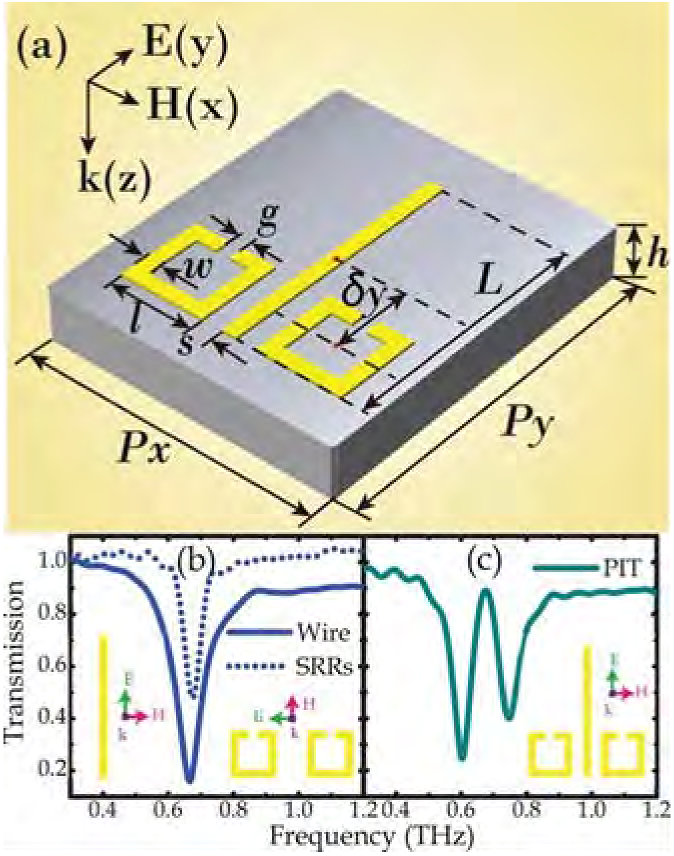

Fig. 8 (a) Schematic diagram of the EIT metamaterial structure with geometrical parameters: Px = 80 *μm*, Py = 20 *μm*, L = 85 *μm*, l = 29 *μm*, s = 7 *μm*, g = 5 *μm*, w = 5 *μm*, and δy = -28 *μm*. Measured amplitude transmissions for (b) sole-wire and sole-SRR pair pattern, and (c) EIT metamaterial comprised of wire and SRR pair in the unit cell [75].

The slow light performance is significantly influenced by the coupling between dark mode and bright mode. This coupling is very sensitive to the space arrangement between these two resonators. For example, it is surprising to see the giant amplitude modulation of the EIT transmission spectra as the SRR pair is gradually displaced from δy = -28 to 28 μm, as depicted in Figs. 9(a) and (d). This is an interesting modulation because no symmetric feature is broken and the distance between the two resonators remains. When the SRRs move upward from δy = -28 to 12 μm, the transparency window gradually shrinks without notable frequency shift. Finally, with a further displacement of δy = 28 μm, the EIT feature completely disappears, leaving behind a broad single resonance dip approaching a minimum transmission of 0.13. The measured tunable spectral response is further supported by full wave numerical simulation using CST Microwave Studio, which is in a good agreement with the measured experimental data.

Actually, it is the interaction between the electrical and magnetic resonances of the SRR resonator that results in this confusing interaction, which we called them electrical pathway and magnetic pathway, respectively. To elucidate this interaction of the electrical and magnetic excitation pathways in further detail, surface current distributions of the electrically and magnetically excited LC resonances are shown in Fig. 10 for samples with δy = -28 and 28 μm due to their opposite behavior. The surface currents in the sample with δy = -28 μm excited by H_z^{Wire} (solid line) and E_x^{Wire} (dashed line) are oscillating in phase. The constructive interference between these two surface currents leads to a strong excitation of the LC resonance in the SRRs, enhancing the coupling between the dark and bright modes. However, when the SRRs move to δy = 28 μm, the magnetically stimulated surface current remains constant but the electrically excited current changes its direction according to the distributions of E_x^{Wire} and H_z^{Wire}. Thus, these two surface currents interact destructively to cancel each other and suppress the excitation of the LC resonance that eventually leads to the disappearance of the EIT peak.

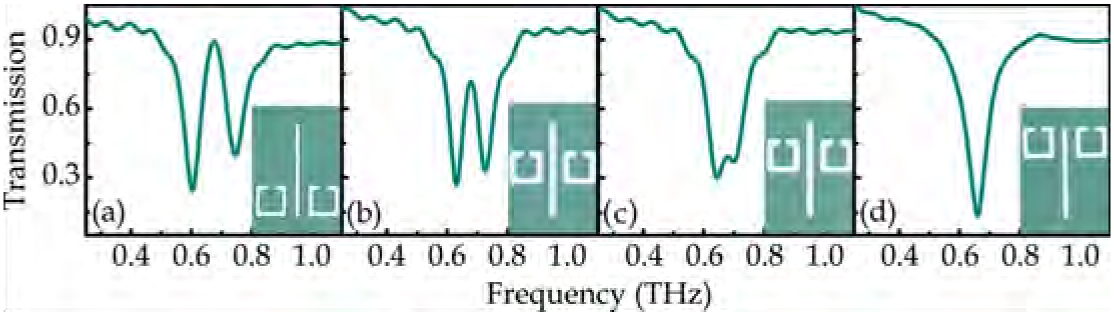

Fig. 9 (a)-(d) Experimental transmission spectra and (e)-(h) corresponding simulated spectra for the SRR pair displacements of δy = -28, 2, 12, and 28 μm, respectively. Inset: microscopic images of the unit cells with different δy [75].

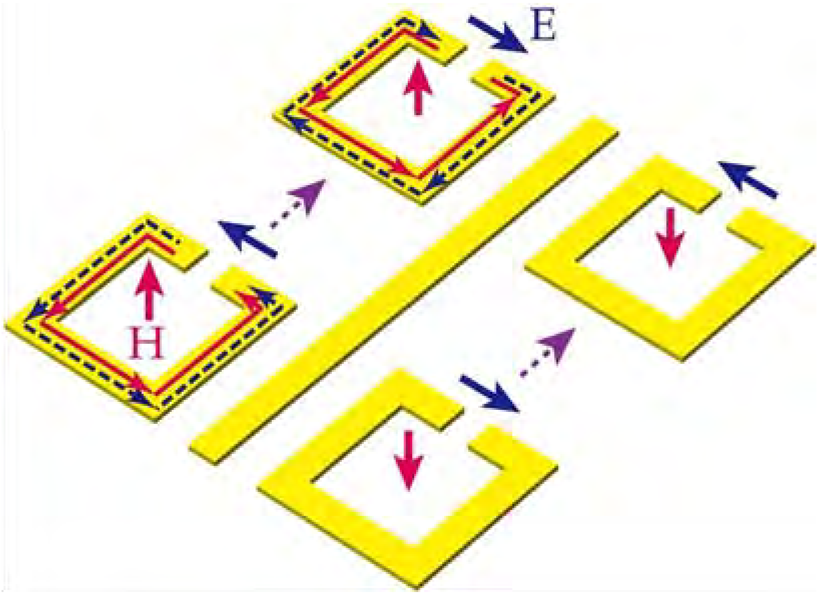

Fig. 10 (a) Surface current distributions of the two excitation pathways on SRRs at δy = -28 and 28 μm.

D. Terahertz cloaking metamaterial

Among all types of metamaterials, invisibility cloak should be the most unique and complex one. Interestingly, this challenge stimulated extensive research enthusiasms. Thanks to transformation optics based on the invariance of Maxwell's equations and plasmonic cancellation based on the Mie scattering theory, the invisibility cloak have been brought into reality in the microwave, terahertz and optical regimes [46, 48, 49, 53, 84-87]. However, there are two factors that shackle the performance of such cloaking devices, namely the extreme optical parameters and inhomogeneity. As such, it has been difficult to go beyond the limitations in bandwidth, intrinsic loss, small dimension of concealed objects and other undesired features arising from metamaterials. Recently, based on a novel cloaking approach only with natural birefringent crystals, we have realized the first macroscopic terahertz cloak. This straightforward method greatly reduces the complexity in design and fabrication of the metamaterial based cloaks. More importantly, the initial works in the visible regime confirmed that this is a promising way towards practical macroscopic cloak devices with frequency and incidence angle robustness.

To cloak the green region as shown in Fig. 11(a), one needs to transform the original space (x,y) shown as the blue triangle in Fig. 11(b) into a new virtual space (x',y'), i.e., the orange region in Fig. 11(a) [53]. Then the green region in Fig. 11(a) is not part of the transformation, or in other words, it is optically cloaked. To simplify the design, we chose the case with TM-polarized terahertz wave in the x-y plane and scaled the permittivity tensor to ensure that the ray trajectories are unchanged for $\mu' = 1$ Thus the parameters are totally nonmagnetic and the dielectric tensor is given as:

$$\overline{\overline{\varepsilon}}' = \begin{pmatrix} 1/\kappa^2 & -\tau/k^2 \\ -\tau/k^2 & 1+\tau^2/\kappa^2 \end{pmatrix} \tag{1}$$

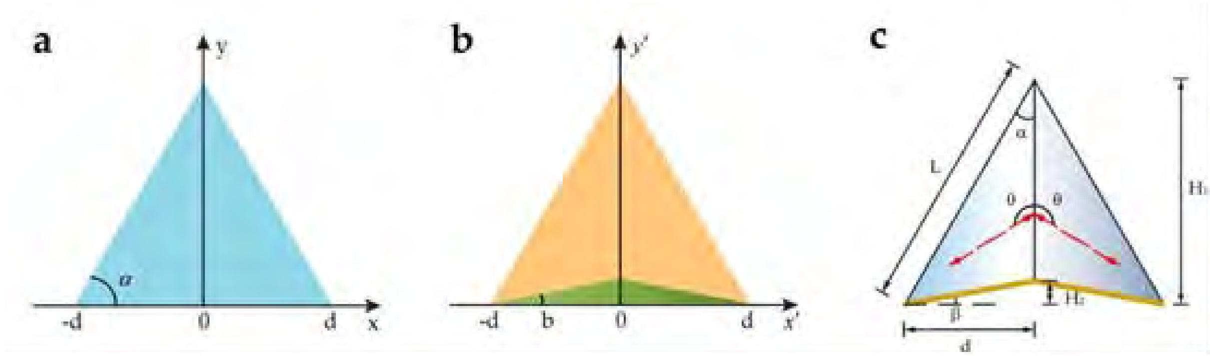

Fig. 11 Illustrations of the coordinate transformation. A quadrilateral region in (a), which is homogeneous and anisotropic is mapped from a triangular cross-section in the original space (b) made from isotropic material. The cloaked region is illustrated as the green triangle in (a), which conceals objects inside. (c) Geometric schematics of the cloak lens [53].

Different from other metamaterials, this design does not need photolithography process. Instead, we compared kinds of reported terahertz birefringent materials to choose one as our cloak device. Finally we found sapphire crystal is the most suitable material with an ordinary n_o and extraordinary light n_e of 3.068 and 3.406 at 0.5 *THz*, respectively. In addition, the absorption and dispersion of sapphire are both extremely low, which is essential in achieving broadband terahertz cloaking. The geometric parameters according to sapphire crystal has a length $L = 40$ *mm* and a height $H_1 = 34.78$ *mm*, respectively, forming a bottom angle $\alpha = 60.4°$, as shown in Fig. 11(c). The height of the cloaking region is $H_2 = 1.75$ *mm*, resulting a cloaking angle $\beta = 5°$. The angle of the crystal axis of sapphire θ is 58.5°.

To obtain the output profiles of the terahertz beam through the sapphire, an angular resolved reflection THz-TDS were utilized as shown in Fig. 12(a). Different from the typical 8-F THz-TDS, a 2-meter-long 800 *nm* single mode fiber was utilized for delivering the ultrafast pumping light onto the detector antenna. Since the cloak is polarization sensitive, three polarizers were added into the system. The Polarizers P1 and P2 were placed in front of the sample to selectively pass the required polarization and P3 was positioned in front of the detector. In the cloaking configuration, the polarization of all three polarizers was parallel to the terahertz electric field. For the reference configuration, P1 and P2 were 45° and 90° oblique from the incident electric field to enable a TE polarized beam. In addition, P3, set at 45°, was combined with the TM polarized detector to receive the refracted TE amplitude signal with a factor of $\sqrt{2}/2$. A schematic diagram of the terahertz cloaking detection and an optical image of the cloak lens are shown in Figs. 12(b) and (c), respectively. The terahertz detector scanned the beam profile in parallel to the output facet of the cloak with a 1-*mm* scan step. As the detector is an incidence angle sensitive receiver, it was rotated at each scan position to ensure the detection of maximum terahertz transient intensity. Subsequently the frequency-dependent terahertz amplitudes at each spatial location were retrieved by Fourier transform of the measured time domain signals.

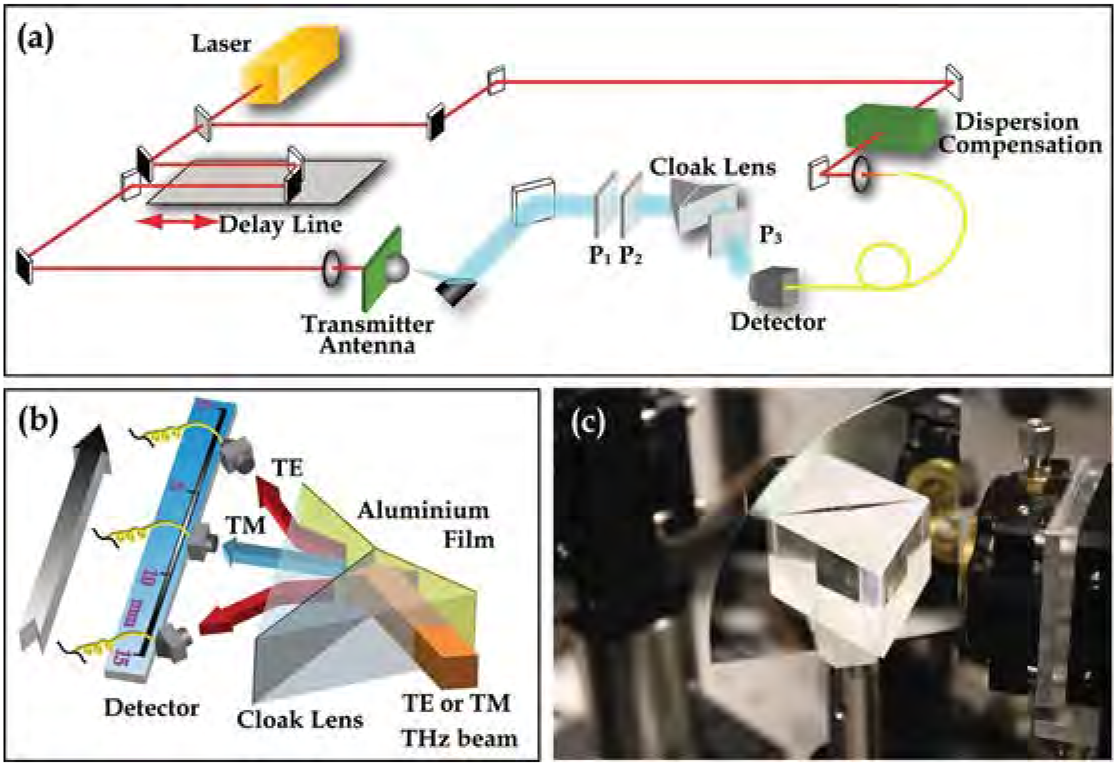

Fig. 12 Schematic diagram of (a) the experiment setup and (b) the cloaking detection; (c) optical image of the mounted cloak lens [53].

In the measurements, the terahertz wave was normally incident (φ_0 = 29.6°) onto the cloak device. Thanks to the time domain mechanism of THz-TDS, a broadband cloaking effect from 0.2 to 1 *THz* can be characterized in a single time-domain measurement at a specific detector location. The Fourier transformed signals were horizontally pixeled with respect to the scan positions, forming the broadband frequency-dependent beam profile maps (Fig. 13). In Fig. 13(a), the reflected TM beam from the cloak shows nearly the same profile as that reflected by a flat mirror (Fig. 13(b)). On the other hand, for the TE beam, the detector received two largely separated beam profiles at the left and right side of the cloaking profile (Fig. 13(c)). For a clear comparison of the output beam profiles among the cloaking, flat surface reflection and reference configuration, the TM and TE measurement results were combined together in Fig. 13(d). It further verifies that the cloak design unambiguously transforms the bump into a flat surface, realizing a large cloaking volume (H_2 = 1.75 *mm*) underneath the lens. Furthermore, the cloaking effect maintains uniformity over a frequency span of 0.8 *THz*.

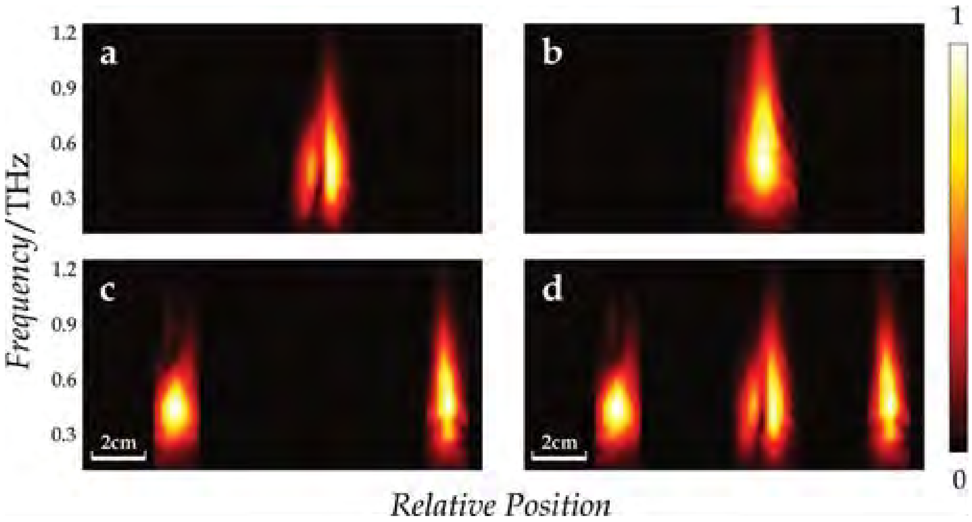

Fig. 13 Experimental results of the cloaking effect with respect to the relative positions (*x* axis) and the frequency (*y* axis). The color represents the relative spectral amplitude: (a) cloaking, (b) flat surface reflection, (c) reference with the same cloak lens, and (d) combined cloaking and reference profiles [53].

Due to the nature of point-to-point mapping in transformation optics, a perfect invisibility cloak should work at all incidence angles. To investigate the angle-dependent cloaking effect, experiments at two other different incidence angles φ_1 =19.6° and φ_2 = 39.6° were carried out for both TE and TM polarizations. The results are shown in Figs. 14(a) and (b) and reveal a robust character when compared with that at φ_0 = 29.6° (Fig. 13(c)). It is obvious that at both oblique incidence angles, the TM-polarized beam shows no deviation in the profile (the central pattern), while a significant splitting was observed with the TE beam.

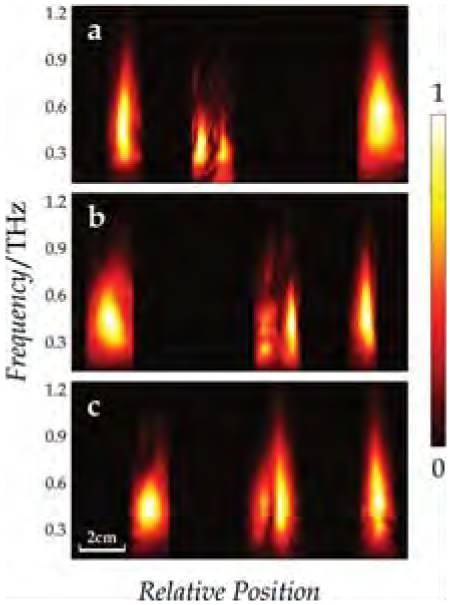

Fig. 14 TE and TM beam profiles with incidence angles: (a) φ_1= 19.6°, (b) φ_2 = 39.6°, and (c) φ_0 = 29.6° [53].

Section IV Active metamaterial terahertz devices

The response of active terahertz metamaterial devices is controlled by external stimulation, which is an important extend of metamaterial based terahertz devices. Generally, the tuning of the response is realized by adding semiconductor, superconductor, and phase-change materials into the structure. Until now, active metamaterial has become a new trend of terahertz metamaterial research.

A. Optically Controlled Terahertz Switch

Usually, active control is employed to alter the fundamental resonance of the SRR structure, which natively exhibits a band-stop behavior in the transmission spectra. More fundamentally, SPPs can resonantly intensify the transmission of electromagnetic energy through subwavelength hole arrays in metallic films, a phenomenon known as extraordinary transmission. When we combined this two structures together on the optical sensitive semiconductors, named silicon on sapphire (SOS), this hybrid metamaterial forms an active terahertz device that presents a resonant transmission that can be dynamically tuned between band-stop or band-pass behaviors.

Figure 15 shows the schematic and a microscopic image of the fabricated structure [88]. The SOS wafer utilized has a 500 *nm* thick silicon layer and a 500 μm thick sapphire substrate. The aluminum SRR array was patterned on the silicon film by using a conventional photolithography process. This was followed by reactive ion etching to form the hole array in the silicon film. Five SRRs and a silicon hole, with dimensions of 33 × 33 μm^2 and 65 × 50 μm^2 respectively, comprise each of the unit cells, as shown in Fig. 19(a), which have a periodicity of 100 × 100 μm^2.

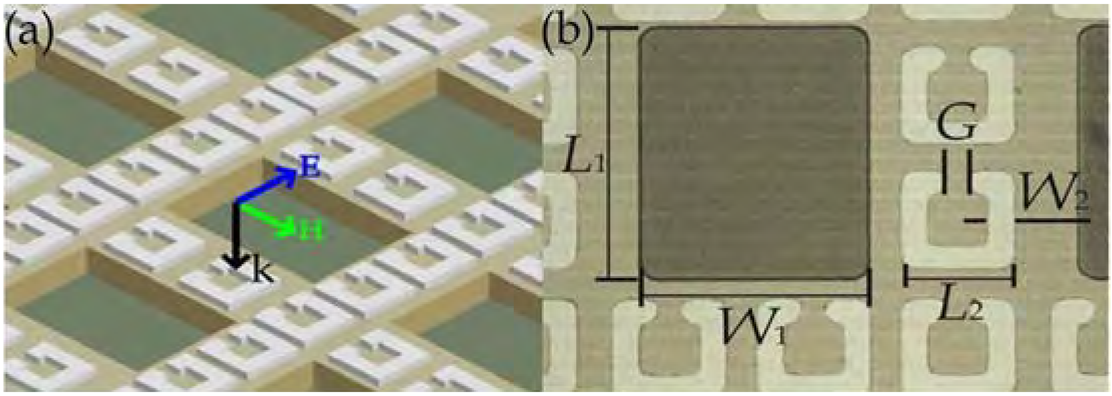

Fig. 15 (a) Schematic and (b) microscopic image of the plasmonic metamaterial (silicon, aluminum and sapphire are marked by yellow, white and green colors, respectively). The geometrical dimensions of the metamaterial are $L_1 = 65\ \mu m$, $W_1 = 50\ \mu m$, $L_2 = 33\ \mu m$, $W_2 = 6\ \mu m$, and $G = 5\ \mu m$ [88].

The optical control of this hybrid metamaterial was verified by an optical pump terahertz probe (OPTP) spectrometer. The output near-infrared laser beam (50 *fs*, 3.2 *mJ* pulse at 800 *nm* with a 1-*kHz* repetition rate) was split into two parts with one being used for terahertz generation detection and the other for optical excitation of the metamaterial samples through a variable neutral density attenuator. The pump beam has a beam diameter of 10 *mm*, much larger than that of the focused terahertz spot (~3 *mm*) at the sample, providing uniform excitation of the metamaterial array. The variation in the pump-probe time delay was implemented using a motion stage through changing the pump beam optical path. Under various pump powers, the transmitted terahertz pulses through the hybrid metamaterials and the blank sapphire reference were measured in the time-domain, thus recording the time-varying electric field of the impulsive terahertz radiation. The transmission amplitude and phase spectra were directly obtained by performing fast Fourier transformation of the time-domain signals and normalized to those of the reference.

Figure 16(a) shows the transmitted spectrum of the hybrid terahertz metamaterial at different pump fluences. The unpumped sample shows the strongest SRR resonance with band-stop transmission amplitude as low as 0.36. When the excitation fluence is gradually increased from 0 to 10 $\mu J/cm^2$, the SRR resonance disappears and the transmission amplitude increases from 0.36 to 0.7. Under 10 $\mu J/cm^2$ excitation the SRR resonance completely disappears and the transmission spectrum shows a flat attenuation. Further increase of the optical fluence up to 255 $\mu J/cm^2$ only reduces the flat amplitude transmission from 0.68 to 0.62 due to increasing photo-carriers in the silicon layer. As the fluence is increased above 255 $\mu J/cm^2$, a resonance peak appears in the transmission spectrum whose amplitude increases with excitation power. The measured peak is attributed to the SPP resonance excited by the semi-metallic silicon hole arrays.

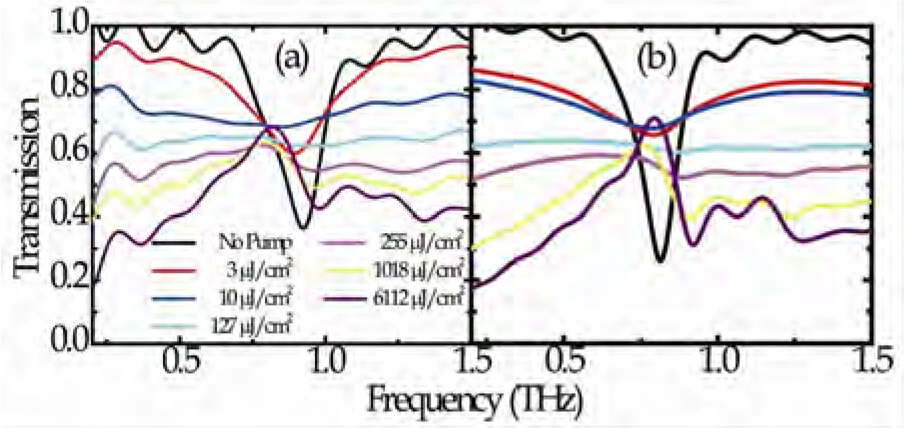

Fig. 16 (a) Measured and (b) simulated transmission spectra at different pump fluences ($\mu J/cm^2$) [88].

Since the tunable response arises from the change in conductivity of the silicon layer, we employed different conductivities in the numerical simulation to represent different pump powers. The simulated amplitude transmissions are shown in Fig. 16(b) which agrees well with the measurements. The electric field distributions at the resonance frequency were simulated for three different conductivities of 0 (no pump), 7.6×10^3 (127 $\mu J/cm^2$), and 2.94×10^5 *S/m* (6112 $\mu J/cm^2$), as shown in Figs. 17(a) - (c), respectively. We clearly observe the transition from high concentration of electric field in the SRR gaps with no pump to intense fields at the edge of the hole arrays with maximum pumping. At the maximum pump fluence the conductivity of the silicon film is high enough to support a SPP resonance. At this pump level the metal SRRs are effectively shorted against the metallic silicon film. The hole array builds up a strong SPP band-pass transmission resonance wherein the electric field is mainly focused along the length of the holes. Interestingly, for moderate pump fluences neither the SRR nor the SPP resonance feature was observed in Fig. 17(b) since the electric field appears to be fairly uniform across the entire sample. The reason is that the conductivity of the silicon layer was enough to damp the SRR resonance but not enough to support the propagation of surface waves, which normally requires some minimum threshold of both metal conductivity and thickness.

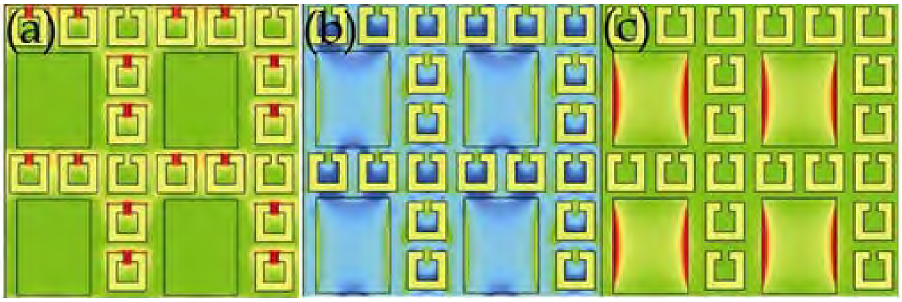

Fig. 17 Simulated electric fields at different pump fluencies ($\mu J/cm^2$): (a) no pump, (b) 127 $\mu J/cm^2$, and (c) 6.11 mJ/cm^2 [88] .

Except optical control of terahertz transmission, recently terahertz delay control also turns to its break through. Still by using SOS wafer, we completed the first optical controlled EIT metamaterial in which the terahertz group index can be tuned. The unit cell of the EIT metamaterial consists of a *CW* and two SRRs, both Al deposited, with Si islands positioned in their gaps by RIE etch, as shown in Fig. 18(a) [54].

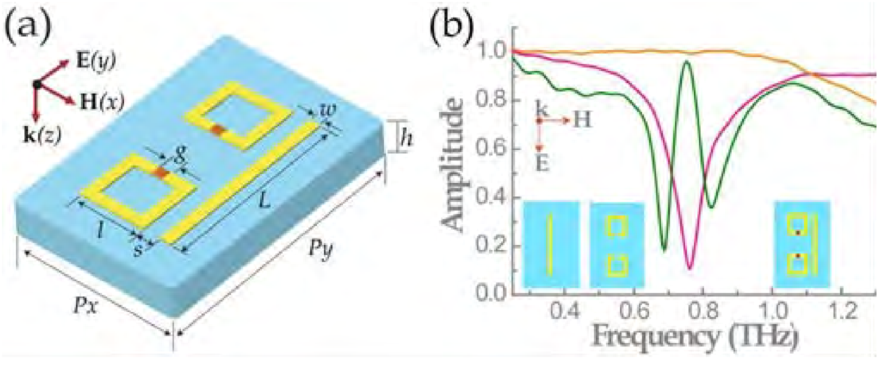

Fig. 18 Experimental design and measured transmission spectra. (a) Schematic of the unit cell. The geometrical parameters are: L = 85, l = 29, s = 7, w = 5, h = 495, g = 5, Px = 80 and Py = 120 μm, respectively. (b) Measured amplitude transmission spectra of the sole-CW (pink), SRR-pair (orange) and the EIT metamaterial sample (olive). The insets in (b) are the structural geometries of the sole-CW, SRR-pair and the EIT metamaterial samples from left to right, respectively, with the polarization illustration [54].

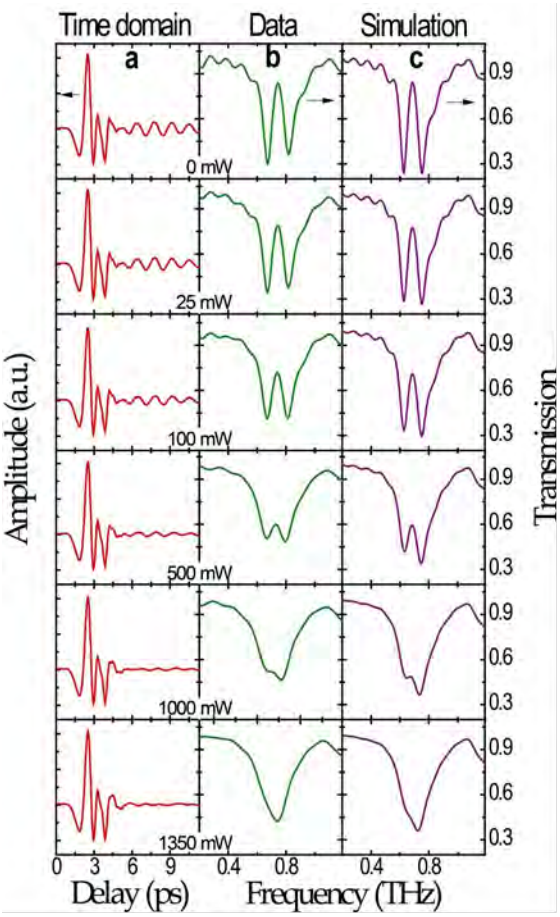

Fig. 19 Active control of the transparency window. (a) Measured transmitted time-domain signals and (b) corresponding normalized Fourier transformed amplitude spectra. (c) Numerical simulation results of normalized spectra of the EIT metamaterial with different conductivities of the Si islands [54].

The transmission property of the EIT sample under different optical excitations is investigated in the OPTP system. The transmitted time-domain pulses and the corresponding normalized amplitude spectra in frequency domain are shown in Fig. 19(a) and (b), respectively. When there is no photoexcitation, a pronounced subsidiary wave packet is observed following the main pulse in the time domain, which is a characteristic of a wave packet with slow group velocity. In the corresponding frequency domain spectrum, an EIT peak is observed between two resonance dips with a transmission amplitude of 85% at 0.74 *THz*. As the excitation power of the pump beam is gradually increased from 25 to 1000 *mW*, the subsidiary wave packet decreases in magnitude, and the corresponding transmission undergoes a strong modulation, as illustrated in Figs. 19(a) and (b), respectively. When the pump power is >1000 *mW*, the transparency window gradually decreases to 50% and the EIT peak vanishes. With the maximum photoexcitation of 1350 *mW*, the time-domain subsidiary packet completely disappears and only a single broad LSP resonance dip as low as 43% is observed in the transmission spectrum, thus completing an on-to-off EIT peak modulation.

In the simulation, the conductivity of the Si islands at the SRR gaps was still varied to simulate the effect of optical excitation, that is, the carrier excitation in the Si islands. As the optical power increased from 0 to 1350 *mW*, the Si conductivity (σ_{Si}) increased from 160 to 4050 *S/m*. The simulation results shown in Fig. 19(c) are in good agreement with the measurements. Clearly, the origin of the EIT resonance modulation essentially comes from the optically tunable conductivity of the Si islands due to the photodoping effect.

Refer to the most important feature of this active EIT control, the tuning of the slow light effect is represented by the group delay (Δt_g) change of the terahertz wave packet through the sample, instead of normally used group refractive index (n_g). The use of Δt_g is more relevant to represent the slow light capability of a device and more importantly, Δt_g retrieval does not require the effective thickness of the sample, which is difficult to define owing to the influence of the substrate on the EIT resonance. The difference in Δt_g through the EIT metamaterial and vacuum with the same thickness is retrieved from their complex transmissions (by Fourier transform) at various photoexcitations, as shown in Fig. 20. The wave packet shown in Fig. 20 with central frequency 0.74 THz is delayed by 5.74 *ps* (including the propagation in the substrate), which is equivalent to the time delay of a 1.72-*mm* distance of free space propagation. However, as the photoexcitation increases to 1350 *mW*, the EIT metamaterial array gradually loses its slow light characteristic, finally turning into a typical LSP group delay feature. To verify the practicality of the tunable EIT metamaterial, an estimated value of ng could be actively tuned from 91 without optical pump to 10.5 at 500 *mW* photoexcitation at 0.74 *THz* with an assumption of 6 *μm* effective sample thickness. This thickness was assumed as the normally polarized electric field amplitude falls below 1/e value of that at the metamaterial surface. The highest n_g representing the slow light tunability is comparable to the previously reported group index values in EIT metamaterials. Most significantly, the active tuning of n_g demonstrated in this work may directly lead to compact, optically controllable slow light devices.

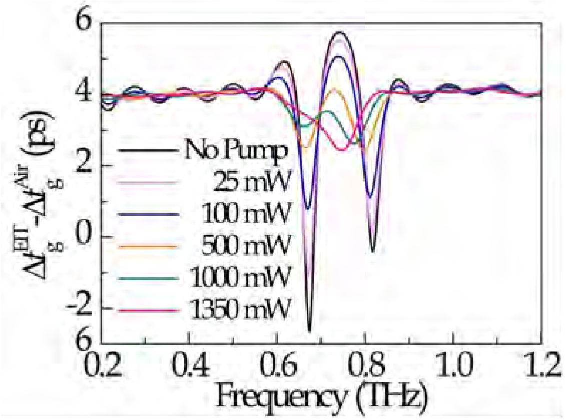

Fig. 20 Optically tunable active group delay. Group delays retrieved from measured transmission spectra under different photoexcitations. Δt_g EIT and Δt_g Air are the group delays through the active EIT metamaterial and vacuum with the same thickness, respectively [54].

B. Temperature controlled superconducting terahertz metamaterial

Temperature control of terahertz metamaterial response is another importance branch in the active metamaterial research field. Refer to terahertz domain, semiconductor, superconductor and phase-shift oxidize material have all been exploited as temperature controlled active metamatetrials. Among these work, high transition temperature (T_c) superconductor such as YBCO attracted much attention because its higher transition temperature and very low Ohmic resistivity at the superconducting state. The unit cell of the first terahertz superconductor metamaterial is been shown in Fig. 21(a). The metamaterial sample was lithographically fabricated from a commercially available 280-*nm*-thick YBCO film which typically has T_c=86 *K* and to a critical current of 2.3 MA/cm^2 maximum current grown on a 500 *nm* thick sapphire substrate (THEVA, Germany). A 3-μm-thick photoresist layer was first patterned on the raw YBCO film as an etching protector. The sample was then wet etched in 0.1% nitric acid for 1 *min* followed by rinsing process in deionized water. The size of the sample array is 5 *mm* × 5 *mm* with SRR periodicity P=52 μm, and the structural dimensions of unit cells are length L = 32 μm, width W = 8 μm, and gap G = 5 μm, as shown in Figs. 21(a).

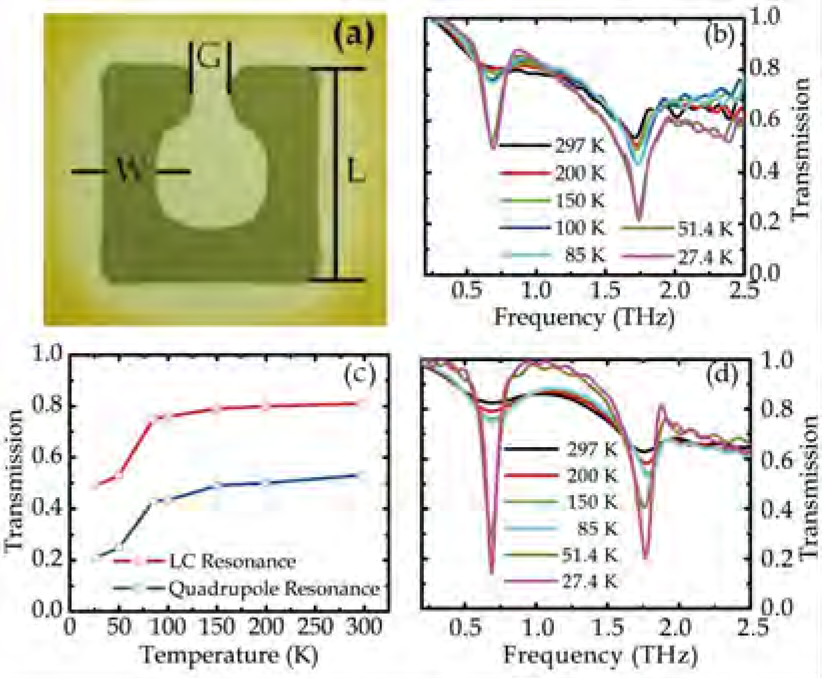

Fig. 21 (a) Microcopic image of YBCO metamaterial unit cell with structural parameters, W = 8 μm, G = 5 μm, and L = 32 μm. (b) Amplitude transmission spectra. (c) Percentage amplitude transmission at different low temperatures. (d) Simulated amplitude transmission spectra of the YBCO metamaterial above and below T_c [62].

The sample was measured in a standard liquid helium cryostat installed in the THz-TDS system. The sample was set with the SRR gap along the incident E field in order to excite the fundamental LC mode resonance and the quadrupole resonance. By filling the vacuum chamber with liquid helium, the sample and the reference were characterized at 297 *K*, 200 *K*, 150 *K*, 100 *K*, 85 *K*, 51.4 *K*, and 27.4 *K*, respectively.

Figure 21(b) shows the temperature-dependent amplitude transmission spectra. At room temperature, the LC and quadrupole resonances appear to be extremely weak due to low conductivity of YBCO. As the temperature is decreased toward T_c, the resonance evolves slowly and becomes more pronounced due to increased current flow in the superconductor film. The resonance shows a switching effect at temperatures lower than T_c. At 27.4 *K*, the LC and quadrupole resonances reach 0.49 and 0.21 with Q factors of 5.3 and 14.5, respectively. Figure 21(c) shows the change in amplitude transmission at the LC and quadrupole resonances with decreasing temperatures. A noteworthy feature is that the sharpest change occurs when the temperature of the YBCO metamaterial is decreased from 85 to 51.4 *K*, thus the transmission at the LC resonance sharply dropping from 0.75 to 0.53. The temperature-dependent amplitude modulation achieved at both the LC and quadrupole resonances is nearly absent in the regular metamaterials composed of thin metal films as the conductivity of metals cannot be modified like that of a system.

The amplitude and phase modulation of the THz transmission primarily originates from the temperature-dependent conductivity in the superconductor metamaterials. According to the two-fluid model, the real part of the conductivity (σ_r) of YBCO is contributed by the normal state carriers whose motion follows Drude model while the imaginary part (σ_r) is determined by the superconducting carriers, which follow the London Equation, 27 where the conductivity of the superconducting carriers can be described as $\sigma_i = i(n_s e^2)/(m^* \omega)$, n_s is the Cooper pair carrier density, *e* is the charge of carriers, m^* is the effective carrier mass, and ω is the frequency of operation. It should be noted that the conductivity due to Cooper pairs is purely imaginary and thus the resistivity of the YBCO below T_c is also nearly imaginary, resulting in an inductor type behavior under the applied THz field. In the THz regime, at temperatures higher than T_c the real part of conductivity is dominant since the absolute value of the imaginary conductivity is three orders of magnitude less than the real part. However, starting from several kelvins under T_c the imaginary conductivity value rises drastically with falling temperatures and the total conductivity is then dominated by σ_i. Previous work on THz conductivity of YBCO film has shown that σ_i increases dramatically and exceeds the real part at several kelvins below T_c. The sharp rise in the imaginary conductivity is signature of the onset of superconductivity and it can serve as an independent method to determine the superconducting T_c. As temperature goes down below T_c, the current in SRR grows stronger due to the superconducting carriers and results in sharp switching at LC and quadrupole resonances. In order to confirm our measurements at temperatures above and well below T_c, finite element simulations were carried out. The simulated amplitude transmission shown in Fig. 21(d) also demonstrates the switching effect at both the resonances as temperature reaches well below T_c at 51.4 and 27.4 *K*. In all, this superconductor metamaterial presents a good terahertz switch capability. In addition, the most fundamental characteristic that makes superconductors attractive for several applications is its ability to carry current without losses, which in future can be one of the paths to minimize the losses in metamaterials.

Section V Conclusion

Metamaterials are novel artificial materials with great flexibility, which satisfy the emergent need of terahertz technology. Here, we presented several metamaterial based terahertz devices, including passive metamaterials whose resonance is determined by the geometric design, and also active metamaterials whose responses can be tuned by external stimulations. The novel characteristics of these metametraials not only present their obvious scientific merit, but also deliver advanced devices such as negative refraction components, broadband filters, slow light optical delay and active tunable devices.

The booming of terahertz metamaterials indeed paves a way to bridge the shortage in terahertz devices. However, there is still a lot to work on toward practical devices. First, for some applications, bulk metamaterials are necessary. Until now, however, three-dimensional fabrication of artificial terahertz structures are far from mature, thus the bulk metamaterial development is much slower than the 2D terahertz counterparts. The second issue is the loss of terahertz metamaterials which is not as low as needed. Basically, the loss comes from three main reasons: Ohmic resistivity in the material, radiative resistivity and the reflection occured at the interface of the device. The radiate resistivity could be reduced by geometric design. Concerning reflection, by combing metamaterial absorber into device design could be a unique way to handle this problem. The reduction of Ohmic loss is very difficult, in the future, however, integrating a gain medium into terahertz metamaterial structure would essentially cancel the influence of Ohmic loss. The last issue is concerning the actively tunable metamaterials. In the view of applications, the reported modulation schemes of the terahertz devices cannot fulfill the requirement of practical environment. Active materials with higher tuning range, faster tuning speed and simpler modulation operation remains as an essential topic in next generation active terahertz metamaterials.

References:

[1] P. H. Siegel. "Terahertz technology". *Microwave Theory and Techniques, IEEE Transactions on*, 50, 910-928 (2002).

[2] M. Tonouchi. "Cutting-edge terahertz technology". *Nature Photon*., 1, 97-105 (2007).

[3] J. F. Federici, B. Schulkin, Feng Huang, et al. "THz imaging and sensing for security applications—explosives, weapons and drugs". *Semiconductor Science and Technology*, 20, S266 (2005).

[4] K. H. Jin, Y.-G. Kim, S. H. Cho, et al. "High-speed terahertz reflection three-dimensional imaging for nondestructive evaluation". *Opt. Express*, 20, 25432-25440 (2012).

[5] M. Tsujimoto, H. Minami, K. Delfanazari, et al. "Terahertz imaging system using high-Tc superconducting oscillation devices". *J. Appl. Phys.*, 111, 123111-4 (2012).

[6] M. Bessou, B. Chassagne, J.-P. Caumes, et al. "Three-dimensional terahertz computed tomography of human bones". *Appl. Opt.*, 51, 6738-6744 (2012).

[7] G. Chen, J. Pei, F. Yang, et al. "Terahertz-Wave Imaging System Based on Backward Wave Oscillator". *Terahertz Science and Technology, IEEE Transactions on*, 2, 504-512 (2012).

[8] P. Jae Yeon, C. Hyuck Jae, N. Gi-Eun, et al. "In Vivo Dual-Modality Terahertz/Magnetic Resonance Imaging Using Superparamagnetic Iron Oxide Nanoparticles as a Dual Contrast Agent". *Terahertz Science and Technology, IEEE Transactions on*, 2, 93-98 (2012).

[9] K. Kyung Won, K. Hyeongmun, P. Jisuk, et al. "Terahertz Tomographic Imaging of Transdermal Drug Delivery". *Terahertz Science and Technology, IEEE Transactions on*, 2, 99-106 (2012).

[10] M.-A. Brun, F. Formanek, A. Yasuda, et al. "Terahertz imaging applied to cancer diagnosis". *Physics in Medicine and Biology*, 55, 4615,

[11] D. L. Woolard, R. Brown, M. Pepper, et al. "Terahertz Frequency Sensing and Imaging: A Time of Reckoning Future Applications?". *Proceedings of the IEEE*, 93, 1722-1743 (2005).

[12] Y. Yang, M. Mandehgar and D. R. Grischkowsky. "Understanding THz Pulse Propagation in the Atmosphere". *Terahertz Science and Technology, IEEE Transactions on*, 2, 406-415 (2012).

[13] Y. Yang, A. Shutler and D. Grischkowsky. "Measurement of the transmission of the atmosphere from 0.2 to 2 *THz*". *Opt. Express*, 19, 8830-8838 (2011).

[14] D. M. Mittleman, R. H. Jacobsen, R. Neelamani, et al. "Gas sensing using terahertz time-domain spectroscopy". *Applied Physics B: Lasers and Optics*, 67, 379-390 (1998).

[15] S. Katletz, M. Pfleger, H. Pühringer, et al. "Polarization sensitive terahertz imaging: detection of birefringence and optical axis". *Opt. Express*, 20, 23025-23035 (2012).

[16] M. J. Paul, J. L. Tomaino, J. W. Kevek, et al. "Terahertz imaging of inhomogeneous electrodynamics in single-layer graphene embedded in dielectrics". *Applied Physics Letters*, 101, 091109-3 (2012).

[17] J. O'Hara, W. Withayachumnankul and I. Al-Naib. "A Review on Thin-film Sensing with Terahertz Waves". *Journal of Infrared, Millimeter, and Terahertz Waves*, 33, 245-291 (2012).

[18] D. Grischkowsky, S. Keiding, M. v. Exter, et al. "Far-infrared time-domain spectroscopy with terahertz beams of dielectrics and semiconductors". *J. Opt. Soc. Am. B*, 7, 2006-2015 (1990).

[19] I. B. Vendik, O. G. Vendik, M. A. Odit, et al. "Tunable Metamaterials for Controlling THz Radiation". *Terahertz Science and Technology, IEEE Transactions on*, 2, 538-549 (2012).

[20] A. L. Bingham and D. R. Grischkowsky. "Terahertz 2-D Photonic Crystal Waveguides". *Microwave and Wireless Components Letters, IEEE*, 18, 428-430 (2008).

[21] A. L. Bingham and D. Grischkowsky. "Terahertz two-dimensional high-Q photonic crystal waveguide cavities". *Opt. Lett*., 33, 348-350 (2008).

[22] Z. Yuguang and D. R. Grischkowsky. "2-D Terahertz Metallic Photonic Crystals in Parallel-Plate Waveguides". *Microwave Theory and Techniques, IEEE Transactions on*, 55, 656-663 (2007).

[23] W. Zhang, A. K. Azad, J. Han, et al. "Direct Observation of a Transition of a Surface Plasmon Resonance from a Photonic Crystal Effect". *Physical Review Letters*, 98, 183901 (2007).

[24] X. Lu, J. Han, and W. Zhang, "Localized Plasmonic Properties of Subwavelength Geometries Resonating at Terahertz Frequencies". *Selected Topics in Quantum Electronics, IEEE Journal of*, 17, 119-129 (2011).

[25] X. Lu, J. Han and W. Zhang. "Resonant terahertz reflection of periodic arrays of subwavelength metallic rectangles". *Applied Physics Letters*, 92, 121103 (2008).

[26] C. Wang, J. Gu, J. Han, et al. "Role of mode coupling on transmission properties of subwavelength composite hole-patch structures". *Applied Physics Letters*, 96, 251102

[27] Z. Tian, A. K. Azad, X. Lu, et al. "Large dynamic resonance transition between surface plasmon and localized surface plasmon modes". *Opt. Express*, 18, 12482-12488

[28] J. Han, A. Lakhtakia, Z. Tian, et al. "Magnetic and magnetothermal tunabilities of subwavelength-hole arrays in a semiconductor sheet". *Opt. Lett*., 34, 1465-1467 (2009).

[29] A. K. Azad, Y. Zhao, W. Zhang, et al. "Effect of dielectric properties of metals on terahertz transmission in subwavelength hole arrays". *Opt. Lett*., 31, 2637-2639 (2006).

[30] A. Azad and W. Zhang. "Resonant terahertz transmission in subwavelength metallic hole arrays of sub-skin-depth thickness". *Opt. Lett*., 30, 2945-2947 (2005).

[31] D. Qu, D. Grischkowsky and W. Zhang. "Terahertz transmission properties of thin, subwavelength metallic holearrays". *Opt. Lett*., 29, 896-898 (2004).

[32] J. G. Rivas, C. Schotsch, P. H. Bolivar, et al. "Enhanced transmission of THz radiation through subwavelength holes". *Physical Review B*, 68, 201306 (2003).

[33] T. J. Yen, W. J. Padilla, N. Fang, et al. "Terahertz Magnetic Response from Artificial Materials". *Science*, 303, 1494-1496 (2004).

[34] H. O. Moser, B. D. F. Casse, O. Wilhelmi, et al. "Terahertz Response of a Microfabricated Rod–Split-Ring-Resonator Electromagnetic Metamaterial". *Physical Review Letters*, 94, 063901 (2005).

[35] S. Linden, C. Enkrich, M. Wegener, et al. "Magnetic Response of Metamaterials at 100 Terahertz". *Science*, 306, 1351-1353 (2004).

[36] A. K. Azad, J. M. Dai and W. L. Zhang. "Transmission properties of terahertz pulses through subwavelength double split-ring resonators". *Optics Letters*, 31, 634-636 (2006).

[37] W. J. Padilla, M. T. Aronsson, C. Highstrete, et al. "Electrically resonant terahertz metamaterials: Theoretical and experimental investigations". *Physical Review B*, 75, 041102 (2007).

[38] R. Singh, A. K. Azad, J. F. O'Hara, et al. "Effect of metal permittivity on resonant properties of terahertz metamaterials". *Optics Letters*, 33, 1506-1508 (2008).

[39] R. Singh, E. Smirnova, A. J. Taylor, et al. "Optically thin terahertz metamaterials". Opt. Express, 16, 6537-6543 (2008).

[40] J. B. Pendry, A. J. Holden, W. J. Stewart, et al. "Extremely Low Frequency Plasmons in Metallic Mesostructures". *Physical Review Letters*, 76, 4773 (1996).

[41] J. B. Pendry, A. J. Holden, D. J. Robbins, et al. "Magnetism from conductors and enhanced nonlinear phenomena". *Microwave Theory and Techniques, IEEE Transactions on*, 47, 2075-2084 (1999).

[42] T. Koschny, M. Kafesaki, E. N. Economou, et al. "Effective Medium Theory of Left-Handed Materials". *Physical Review Letters*, 93, 107402 (2004).

[43] J. B. Pendry. "Negative Refraction Makes a Perfect Lens". *Physical Review Letters*, 85, 3966 (2000).

[44] J. Chen, Y. Wang, B. Jia, et al. "Observation of the inverse Doppler effect in negative-index materials at optical frequencies". *Nature Photon.*, 5, 239-245 (2011).

[45] J. B. Pendry, A. Aubry, D. R. Smith, et al. "Transformation Optics and Subwavelength Control of Light". *Science*, 337, 549-552 (2012).

[46] X. Chen, Y. Luo, J. Zhang, et al. "Macroscopic invisibility cloaking of visible light", *Nat. Commun.*, 2, 176 (2011).

[47] J. B. Pendry, D. Schurig and D. R. Smith. "Controlling Electromagnetic Fields". *Science*, 1125907 (2006).

[48] D. Schurig, J. J. Mock, B. J. Justice, et al. "Metamaterial Electromagnetic Cloak at Microwave Frequencies". *Science*, 314, 977-980 (2006).

[49] T. Ergin, N. Stenger, P. Brenner, et al. "Three-Dimensional Invisibility Cloak at Optical Wavelengths". *Science*, 328, 337-339

[50] A. J. Danner, T. Tyc and U. Leonhardt. "Controlling birefringence in dielectrics". *Nature Photon.*, 5, 357-359 (2011).

[51] U. Leonhardt and T. Tyc. "Broadband Invisibility by Non-Euclidean Cloaking". *Science*, 323, 110-112 (2009).

[52] U. Leonhardt. "Optical conformal mapping". *Science*, 312, 1777-1780 (2006).

[53] D. Liang, J. Gu, J. Han, et al. "Robust Large Dimension Terahertz Cloaking". *Advanced Materials*, 24, 916-921 (2012).

[54] J. Gu, R. Singh, X. Liu, et al. "Active control of electromagnetically induced transparency analogue in terahertz metamaterials". *Nat. Commun.*, 3, 1151 (2012).

[55] S. Zhang, J. Zhou, Y.-S. Park, et al. "Photoinduced handedness switching in terahertz chiral metamolecules". *Nat. Commun.*, 3, 942 (2012).

[56] S. H. Lee, M. Choi, T.-T. Kim, et al. "Switching terahertz waves with gate-controlled active graphene metamaterials". *Nature Mater.*, 11, 936-941 (2012).

[57] H.-T. Chen, J. F. O'Hara, A. K. Azad, et al. "Experimental demonstration of frequency-agile terahertz metamaterials". *Nature Photon.*, 2, 295-298 (2008).

[58] H.-T. Chen, W. J. Padilla, M. J. Cich, et al. "A metamaterial solid-state terahertz phase modulator". *Nature Photon.*, 3, 148-151 (2009).

[59] H.-T. Chen, W. J. Padilla, J. M. O. Zide, et al., "Active terahertz metamaterial devices". *Nature*, 444, 597-600 (2006).

[60] J. Han, A. Lakhtakia and C.-W. Qiu. "Terahertz metamaterials with semiconductor split-ring resonators for magnetostatic tunability". *Opt. Express*, 16, 14390-14396 (2008).

[61] T. Driscoll, H.-T. Kim, B.-G. Chae, et al. "Memory Metamaterials". *Science*, 325, 1518-1521 (2009).

[62] J. Gu, R. Singh, Z. Tian, et al. "Terahertz superconductor metamaterial". *Applied Physics Letters*, 97, 071102 (2010).

[63] A. K. Azad, Y. Zhao and W. Zhang. "Transmission properties of terahertz pulses through an ultrathin subwavelength silicon hole array", *Applied Physics Letters*, 86, 141102 (2005).

[64] G. V. Viktor. "The electrodynamics of substances with simultaneously negative values of ϵ and μ". *Soviet Physics Uspekhi*, 10, 509-514 (1968).

[65] S. Zhang, Y.-S. Park, J. Li, et al. "Negative Refractive Index in Chiral Metamaterials". *Physical Review Letters*, 102, 023901 (2009).

[66] M. Awad, M. Nagel and H. Kurz. "Negative-index metamaterial with polymer-embedded wire-pair structures at terahertz frequencies". *Opt. Lett.*, 33, 2683-2685 (2008).

[67] O. Paul, C. Imhof, B. Reinhard, et al. "Negative index bulk metamaterial at terahertz frequencies". *Opt. Express,* 16, 6736-6744 (2008).

[68] J. Gu, J. Han, X. Lu, et al. "A close-ring pair terahertz metamaterial resonating at normal incidence". *Opt. Express*, 17, 20307-20312 (2009).

[69] X. Zhang, J. Gu, W. Cao, et al. "Bilayer-fish-scale ultrabroad terahertz bandpass filter". *Opt. Lett.*, 37, 906-908 (2012).

[70] M. E. MacDonald, A. Alexanian, R. A. York, et al. "Spectral transmittance of lossy printed resonant-grid terahertz bandpass filters". *Microwave Theory and Techniques, IEEE Transactions on*, 48, 712-718 (2000).

[71] Y.-J. Chiang, C.-S. Yang, Y.-H. Yang, et al. "An ultrabroad terahertz bandpass filter based on multiple-resonance excitation of a composite metamaterial". *Applied Physics Letters*, 99, 191909 (2011).

[72] M. Lu, W. Li and E. R. Brown. "Second-order bandpass terahertz filter achieved by multilayer complementary metamaterial structures". *Opt. Lett.*, 36, 1071-1073 (2011).

[73] Y. Zhu, S. Vegesna, V. Kuryatkov, et al. "Terahertz bandpass filters using double-stacked metamaterial layers". *Opt. Lett.*, 37, 296-298 (2012).

[74] J. Han, J. Gu, X. Lu, et al. "Broadband resonant terahertz transmission in a composite metal-dielectric structure". *Opt. Express*, 17, 16527-16534 (2009).

[75] X. Liu, J. Gu, R. Singh, et al. "Electromagnetically induced transparency in terahertz plasmonic metamaterials via dual excitation pathways of the dark mode". *Applied Physics Letters*, 100, 131101 (2012).

[76] T. Driscoll, G. O. Andreev, D. N. Basov, et al. "Quantitative investigation of a terahertz artificial magnetic resonance using oblique angle spectroscopy". *Applied Physics Letters*, 90, 092508 (2007).

[77] N. Liu, T. Weiss, M. Mesch, et al. "Planar Metamaterial Analogue of Electromagnetically Induced Transparency for Plasmonic Sensing". *Nano Letters*, 10, 1103-1107 (2010).

[78] C. Kurter, P. Tassin, L. Zhang, et al. "Classical Analogue of Electromagnetically Induced Transparency with a Metal-Superconductor Hybrid Metamaterial". *Physical Review Letters*, 107 (2011).

[79] N. Liu, L. Langguth, T. Weiss, et al. "Plasmonic EIT at the Drude damping limit". *2009 Conference on Lasers and Electro-Optics and Quantum Electronics and Laser Science Conference (Cleo/Qels 2009)*, 1-5, 2019-2020 (2009).

[80] R. Singh, C. Rockstuhl, F. Lederer, et al. "Coupling between a dark and a bright eigenmode in a terahertz metamaterial". *Physical Review B*, 79, 4 (2009).

[81] S.-Y. Chiam, R. Singh, C. Rockstuhl, et al. "Analogue of electromagnetically induced transparency in a terahertz metamaterial". *Physical Review B*, 80, 153103 (2009).

[82] P. Tassin, L. Zhang, T. Koschny, et al. "Low-Loss Metamaterials Based on Classical Electromagnetically Induced Transparency". *Physical Review Letters*, 102, 053901 (2009).

[83] S. Zhang, D. A. Genov, Y. Wang, et al. "Plasmon-Induced Transparency in Metamaterials". *Physical Review Letters*, 101, 047401 (2008).

[84] F. Zhou, Y. Bao, W. Cao, et al. "Hiding a Realistic Object Using a Broadband Terahertz Invisibility Cloak". *Sci. Rep.*, 1, 78 (2011).

[85] B. Zhang, Y. Luo, X. Liu, et al. "Macroscopic Invisibility Cloak for Visible Light". *Physical Review Letters*, 106, 033901 (2011).

[86] H. F. Ma and T. J. Cui. "Three-dimensional broadband ground-plane cloak made of metamaterials". *Nat. Commun*., 1, 21 (2010)

[87] J. Valentine, J. Li, T. Zentgraf, et al. "An optical cloak made of dielectrics". *Nature Mater*., 8, 568-571 (2009).

[88] J. Gu, R. Singh, A. K. Azad, et al. "An active hybrid plasmonic metamaterial". *Opt. Mater. Express*, 2, 31-37 (2012).